Desalination and Water Treatment
www.deswater.com

doi: 10.5004/dwt.2021.26607

211 (2021) 280–295
January

Two-dimensional MXene for efficient arsenic removal from aqueous solutions: experimental and molecular dynamics simulation

Ahmad Kayvani Fard[a,*], Tarik Rhadfi[a], Gordon McKay[b], Yehia Manawi[a], Viktor Kochkodan[a], One-Sun Lee[a], Muataz A. Atieh[c,d,*]

[a]*Qatar Environment and Energy Research Institute, Hamad Bin Khalifa University, P.O. Box: 5825, Doha, Qatar, Fax: +974 44540487; email: afard@hbku.edu.qa (A.K. Fard), Fax: +974 44541528; emails: mhussien@qf.org.qa (M. Ali Atieh), trhadfi@hbku.edu.qa (T. Rhadfi), ymanawi@hbku.edu.qa (Y. Manawi), vkochkodan@hbku.edu.qa (V. Kochkodan), olee@hbku.edu.qa (O.-S. Lee)*
[b]*Division of Sustainable Development, College of Science and Engineering, Hamad Bin Khalifa University, Qatar Foundation, P.O. Box: 5825, Doha, Qatar, email: gmckay@hbku.edu.qa*
[c]*College of Engineering, University of Sharjah, P.O. Box: 27272, Sharjah, United Arab Emirates, email: mhussien@sharjah.ac.ae*
[d]*Desalination Research Group, Research Institute of Sciences and Engineering, University of Sharjah, Sharjah, P.O. Box: 27272, United Arab Emirates*

Received 31 March 2020; Accepted 20 September 2020

ABSTRACT

MXene as a new type of metal carbide was used as a nanoadsorbent for the removal of toxic arsenic species from water. It was prepared by etching the Ti_3C_2Al powders in HF solution. The final product was (2D) titanium carbide nanosheet. The prepared MXene exhibited high sorption capacities and fast kinetics for As(III) removal from water. It provided an efficient removal performance for As(III) with a capacity of 2.8 mg/g, higher than most of the commercial adsorbents. The residual concentration of As in water is far below the standard limit set by World Health Organization for drinking water at 10 μg/L. Using steered molecular dynamics simulation, the global minimum energy between arsenic and MXene surface was found to be of 7.1 kJ/mol. The arsenic adsorption data with MXene fits very well the pseudo-second-order model with a coefficient of determination being close to unity. The second-order rate constant was (k_2) found to be 25.38 g/mgh and adsorption capacity was found to be 0.241 mg/g. Furthermore, MXene nanosheets were also discovered to remove other contaminants, such as Cr(VI), Ba(II) and Pb(II) from water. These significantly expand the potential applications of 2D $Ti_3C_2T_x$ nanosheets in water treatment due to their well-defined morphology, which holds promising industrial advantages.

Keywords: Titanium carbide; MXene; Adsorption; Arsenic; 2D nanomaterial; Molecular dynamics simulation

1. Introduction

Arsenic pollution in water is one of the major issues around the globe. Arsenic occurs naturally in the environment as a tasteless, semi-metal, and odorless element. Arsenic can also occur through anthropogenic sources by industrial and agricultural activities. The maximum contaminant level for arsenic in drinking water, as set in provisional guidelines by the World Health Organization, is 10 μg/L [1]. Long and chronic exposure to arsenic is associated with numerous health problems such as different types of cancers, arsenicosis, kidney, skin, and lung problems [2,3]. With its complex chemistry, arsenic in neutral water exists as an oxoanion in two dominant forms: arsenite (As(III)) and arsenate (As(V)) [4–6]. Depending on the pH of the solution, As(V) exists as AsO_4^{3-}, $HAsO_4^{2-}$, H_2AsO^{4-}, and H_3AsO_4 and As(III) exists as $As(OH)_3$, $As(OH)_4^-$, $H_2AsO_3^-$, $HAsO_3^{2-}$, $AsO_2OH^{2-}$and AsO_3^{3-} in an aqueous solution [2].

* Corresponding author.

As(III) is considered to be a hard acid and mostly forms complexes with oxides and nitrogen, while As(V) acts as soft acid, typically forming complexes with sulfides. Due to their unique chemistry, the oxoanion properties allow arsenic and its derivatives to interact with other metal hydroxide surfaces through the formation of monodentate and bidentate inner surface complexes, thus, rendering such media suitable for removing elements such as arsenic by adsorption [7].

Different removal techniques are introduced for the removal of As(III) and As(V) in which a few are frequently used to treat wastewater and contaminated drinking water. Coagulation, oxidation/chemical precipitation, ion exchange, reverse osmosis, and adsorption are examples of some removal techniques that are currently employed. However, these techniques have drawbacks and restrictions in their application. For instance, chemical oxidation and precipitation is achieved by the addition of chemical reagents followed by the separation of the treated water and the precipitated solids. This method will leave behind the effects of both reagent addition and the production of sludge. While membrane processes, such as reverse osmosis, are very efficient in removing arsenic from water, they are prone to fouling and require frequent cleaning or replacement, which is a costly process. Ion exchange releases harmful chemicals into the environment, and adsorption is limited to the affinity of the adsorbent for the adsorbate [8–10].

Among all of these techniques, adsorption has generated the most attention for the removal of heavy metals, specifically arsenic, from industrial wastewater. Selective adsorption processes use mineral oxides, polymeric resins, biological materials, and activated carbon. Activated carbon is widely used due to its high surface area and high porosity. Other studied media for the adsorption of arsenic includes activated alumina [11,12], zeolite [13], sand [14], iron hydroxide and oxide [15–18], silica and phyllosilicates [19], and cellulose sponge [20]. Other than the surface area, other properties such as adsorbent and adsorbate chemical properties, pH, ionic strength, and temperature have an effect on adsorption and adsorption capacity of the material [2].

In this study, we present a novel two-dimensional (2D) carbon nanomaterial to be implemented as a unique adsorbent. This nanomaterial lies under the group of nanolaminated ternary carbides and nitrides known as the MAX phase. The chemical formula typically used for these carbides and nitrides is $M_{n+1}AX_n$, where n = 1, 2, or 3, M is an early transition metal (such as Ti, Cr, V, Nb, etc.), A is an A-group element (such as Sn, Al, Si, In, etc.), and X is either a carbon or nitrogen. Titanium(III) carbide(II) (Ti_3C_2), a member of the MAX family and commonly known as MXene, is applied in this study as a novel adsorbent nanomaterial. MXenes have generated wide interest due to their physical and chemical stabilities, hydrophilicity, exceptional electrical conductivity, and environmental-friendliness [21,22].

Several research studies implementing MXenes have been conducted in areas such as catalysis, energy storage, sensors, and membranes for water treatment [23]. Novoselov et al. [24] attributed the wide application of MXenes to their ability to host and intercalate several cations, such as Li^+, Na^+, Mg^{2+}, K^+, and NH_4^+ within the Ti_3C_2 layer in aqueous solutions. Recently, MXenes and their derivatives have generated wide interest for the removal of contaminants from water for wastewater treatment applications [21,23,25–28]. More information on the perspectives and challenges of MXene application for water treatment and remediation can be found in recent reviews [29,27,28].

For the first time, we present herein the application of 2D MXene nanosheets for the removal of As(III) from water. As(III) adsorption kinetics and adsorption isotherms were studied to identify the adsorption mechanism. To further establish the interaction between arsenic and MXenes, Steered molecular dynamics (SMD) simulation was employed. The use of SMD is crucial in identifying the binding energy between arsenic and MXenes since available numerical models in literature are developed mainly for gases and macroporous materials.

2. Materials and methods

2.1. Materials

MXenes, having the chemical formula of Ti_3C_2 were prepared by a method found elsewhere [30] via the exfoliation of titanium(III) aluminium carbide(II) Ti_3AlC_2 at room temperature using hydrofluoric (HF) acid according to the following reactions (Fig. 1):

$$Ti_3AlC_2 + 3HF \rightarrow AlF_3 + \frac{3}{2}H_2 + Ti_3C_2 \quad (1)$$

$$Ti_3C_2 + 2H_2O \rightarrow Ti_3C_2(OH)_2 + H_2 \quad (2)$$

$$Ti_3C_2 + 2HF \rightarrow Ti_3C_2F_3 + H_2 \quad (3)$$

In brief, the MAX phase (Ti_3AlC_2) was synthesized by mixing commercial Ti_2AlC and TiC at a molar ratio of 1:1 using a ball-mill for 20 h. The MAX phase was then sintered under an inert environment using a tube furnace up to 1,300°C at a heating rate of 5°C/min. The resulting powder was then exfoliated using 50 wt.% HF to selectively remove the Al layer from the sintered MAX phase, producing $Ti_3C_2T_x$. The agglomerated MXene ($Ti_3C_2T_x$) powder was then dispersed in ethanol solution and ultra-sonicated for 1 h at 60% amplitude under an inert atmosphere of argon. The dispersed $Ti_3C_2T_x$ nanosheets were separated and collected using centrifugation followed by drying overnight.

All chemicals used in this study were reagent grade. Stock solutions of As(III) were prepared from a 1,000 mg/L As(III) in nitric acid solution (TraceCERT® [Sigma-Aldrich]). The pH of the solutions was adjusted using analytical grade HCl (36.5%–38.0% purity, VWR International) and NaOH (ACS reagent, ≥97.0%, pellets, VWR International) solutions. In this context, and for the sake of simplicity, all $Ti_3C_2T_x$ notation has been replaced by MXene.

2.2. Methods

2.2.1. Chemical analysis

The arsenic concentration in water was analyzed using a Bruker Aurora Elite Inductive Coupled Plasma-Mass Spectrometer (ICP-MS). To prepare the samples for analysis,

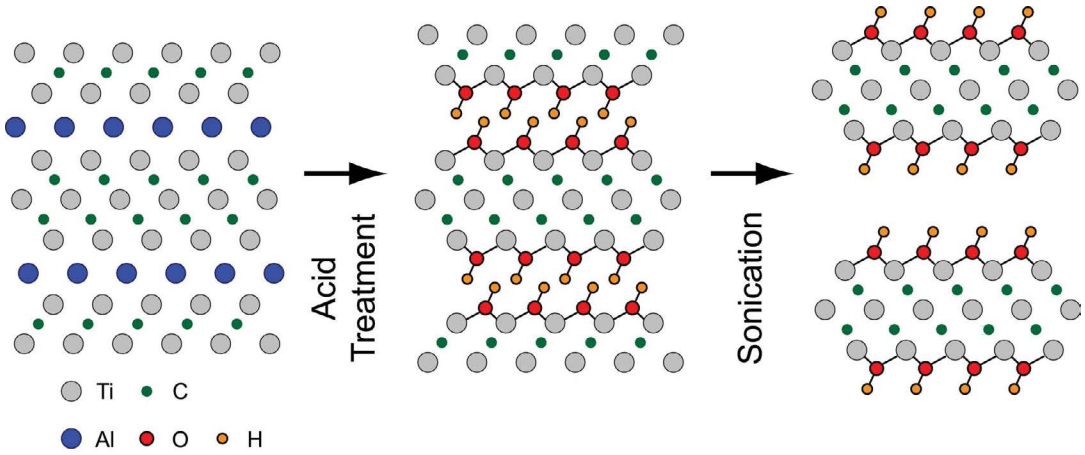

Fig. 1. Exfoliation and sonication of MAX to synthesize MXene.

the untreated and treated water samples were preserved and diluted 100 times with 1% w/w HNO_3/H_2O prior to analysis. The arsenic concentration was analyzed in a helium collision mode (67 mL/min) using a dwell time of 30 ms, 10 replicates and a plasma power of 1,450 W.

2.2.2. Characterization techniques

The surface imaging of the MXene sample was performed via field-emission scanning electron microscopy (FE-SEM; JEOL JSM-7610F [JEOL Inc. Japan]) combined with an energy dispersive X-ray spectroscopy (EDS) unit (OXFORD instruments, INCAx-Max20, United Kingdom) for elemental analysis. The zeta potential of the MXenes was measured at room temperature (25°C) using a Zetasizer instrument (Nano ZS90, Malvern Instruments Ltd., Malvern, UK) equipped with a 4.0 mW internal laser, functioning on the principle of dynamic light scattering and with a scattering angle of 90°. Powder X-ray diffraction (XRD) patterns were measured using a Rigaku MiniFlex-600 instrument (40 kV and 15 mA) at a Cu Kα radiation (λ = 1.54 Å) and a rate of 0.4% over Bragg angles ranging from 10° to 90°. The surface area of the MXenes was measured by N_2 adsorption at 77 K using a BET surface area analyzer (Micrometrics ASAP 2020). Finally, the physical and chemical properties of the MXenes with respect to temperature were investigated using thermogravimetric analysis (TGA; SDT, Q600, TA Instruments) with a heating rate of 10°C/min under argon from room temperature to 1,350°C.

2.2.3. Batch experimental studies

Arsenic removal experiments were carried out in batch mode. The required arsenic concentration was prepared by diluting an arsenic standard solution (1,000 mg/L). All experiments were conducted in triplicates at room temperature. The adsorption capacity and removal efficiency were calculated as follows:

$$Q = \frac{\left(C_i - C_f\right) \times V}{W_g} \tag{4}$$

$$\text{RE}(\%) = \frac{\left(C_i - C_f\right)}{C_i} \times 100 \tag{5}$$

where C_i (mg/L) is the initial concentration of arsenic in the water, C_f (mg/L) is the residual arsenic concentration in the water, V (L) is the volume of the water, and W_g is the mass of MXenes.

To examine the effect of pH on the removal efficiency and adsorption capacity, experiments using various MXene loadings were conducted in 50 mL polypropylene conical tubes containing 20 mL As(III) solution at a concentration of 1 ppm. The tubes were shaken using a mechanical shaker at a speed of 100 rpm. Experiments investigating the effect of contact time on the removal efficiency of As(III) were conducted using 1 ppm arsenic solution, 100 mg MXenes and at varying pH values. Samples at each time interval were collected and analyzed for arsenic using ICP-MS.

2.3. Isotherm and kinetic models

Adsorption isotherm experiments were conducted at varying initial As(III) concentrations while keeping all other parameters similar to those mentioned in Section 2.2. The experimental data in this section were validated using various existing models such as Freundlich, Langmuir, and Dubinin–Radushkevich (D-R) isotherm models. The linear Freundlich isotherm model is expressed as:

$$\ln Q_e = \ln K_F + \frac{1}{n} \ln C_e \tag{6}$$

where C_e is the arsenic concentration at equilibrium (mg/L), Q_e is the adsorption capacity at equilibrium, and n and K_F are Freundlich empirical constants related to the sorption intensity and the sorption capacity of the adsorbent, respectively.

The Langmuir isotherm model assumes that the adsorption takes place at defined homogeneous sites on the surface of the adsorbent. The linearized form of the Langmuir isotherm is expressed by the equation:

$$\frac{C_e}{Q_e} = \frac{1}{X_m K} + \frac{C_e}{X_m} \tag{7}$$

where K is the Langmuir constant and X_m is the maximum arsenic adsorption capacity (mg/g).

To estimate the adsorption mechanism with a Gaussian energy distribution onto a heterogeneous surface, the Dubinin–Radushkevich isotherm is generally used [31,32]. The linearized form of the model is expressed as:

$$\ln Q_e = \ln Q_m - \beta\varepsilon^2 \tag{8}$$

where B is Dubinin–Radushkevich isotherm parameter (mol²/kJ²) and ε is Dubinin–Radushkevich isotherm constant and expanded as:

$$\varepsilon = RT\ln\left(1 + \frac{1}{C_e}\right) \tag{9}$$

The mean free energy denoted as E_α per ion of arsenic is then calculated:

$$E_\alpha = \frac{1}{\sqrt{2B}} \tag{10}$$

Experimental data obtained from the kinetic experiments were correlated with established kinetic models such as the pseudo-first-order and pseudo-second-order models.

The Lagergren pseudo-first-order model proposes that the rate of sorption is proportional to the number of sites unoccupied by the adsorbate [33]. The linearized form of the pseudo-first-order equation can be expressed as:

$$\ln\left(Q_e - Q_t\right) = \ln Q_e - k_1 t \tag{11}$$

where Q_t is the sorption capacity (mg/g) at any preset time interval (t) and k_1 is the first-order rate constant (min⁻¹) [34]. The pseudo-second-order kinetic model can be written in a linearized form as follows:

$$\frac{t}{Q_t} = \frac{1}{k_2 Q_e^2} + \frac{t}{Q_e} \tag{12}$$

where k_2 is the second-order rate constant (g/mg min). From the intercept and slope of the (t/Q_t) vs. t plot, k_2 and Q_e can be determined, respectively.

2.4. SMD simulations

To validate the binding energy found using D-R isotherm, SMD simulation was used. The system for calculating the adsorption energy of arsenous acid on the surface of MXene is shown in Fig. 2. The system was composed of a section of MXene with dimensions of 27 × 23 × 8 Å³ and the arsenous acid. The SPC/E model of water was adapted for solvating the system [35], and the number of water molecules in the simulation box was 2,219 with the initial dimensions of the system being 40 × 40 × 50 Å³.

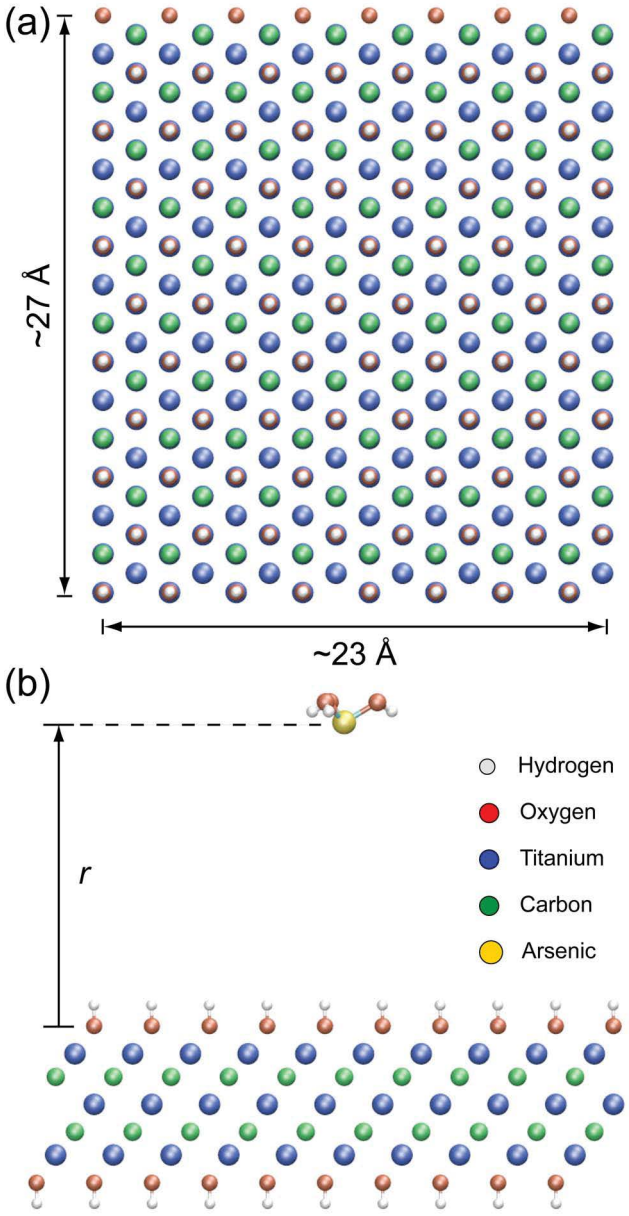

Fig. 2. (a) Top view of MXene used in the simulation of this report. (b) The distance between the surface of oxygen of MXene and the arsenic atom is obtained calculating the adsorption energy of arsenous acid. Water molecules are not shown for clarity.

The potential of the mean force (PMF) was also calculated for the adsorption of arsenous acid on the surface of MXene using SMD [36–42]. During SMD simulation, the positions of titanium, carbon, and oxygen of MXene are fixed by applying harmonic constraint while the arsenous acid is pulled with a constant velocity of 1.0 Å/ns along the orthogonal axis to the surface of MXene. A harmonic constraint with a spring constant of 10 kcal/mol/Å² is used for pulling the arsenic atom, and the total length of the pulling reaction coordinate was 12.0 Å. The reaction coordinate was divided into three consecutive sections ((2 ≤ r ≤ 6,

$6 \le r \le 10$, and $10 \le r \le 14$)) with each section length of 4 Å, and adapting the matching relation to assemble each PMF profile [43]. At each section, the system was equilibrated for 200 ps while constraining the position of MXene and arsenic, and SMD simulation data were collected during another 4 ns. Eight independent simulations were performed at each section for constructing the PMF. We adopted the Jarzynski [44,45] equation to construct the PMF from SMD simulations.

$$\Delta A = -\beta^{-1} \ln\left\langle -\beta W \right\rangle \tag{13}$$

where ΔA is a free energy difference, β is the product of the Boltzmann factor and temperature, and W is the non-equilibrium work obtained from the SMD simulation. With Eq. (10), the non-equilibrium work done by the pulling force was obtained and expressed in Eq. (11):

$$W = -k\nu \int_0^t dt' \left[r\left(t'\right) - r_0 - \nu t' \right] \tag{14}$$

where k is the force constant and ν is the velocity of pulling. The reaction coordinate at t' is $r(t')$ and the initial position of arsenic is r_0. The second-order cumulant expansion Eq. (12) was adopted for calculating Eq. (10) [37,38].

$$\Delta A = \left\langle W \right\rangle - \frac{\beta}{2}\left[\left\langle W^2 \right\rangle - \left\langle W \right\rangle^2 \right] \tag{15}$$

All the SMD simulations were performed using the NPT ensemble at 300 K with a damping coefficient of 5 ps^{-1} of Langevin dynamics [46]. The Langevin piston method, with a 100 fs piston period, was adapted to keep the pressure at 1 atm (damping time constant was 50 fs and piston temperature was 300 K) [46,47]. With the particle mesh Ewald method, full electrostatics was employed with a 1 Å grid width [48]. Using a group based cutoff, nonbonded interactions were updated every 10 time steps, SETTLE algorithm [49] was used to hold rigid covalent bonds involving hydrogen. A 1 fs time step was used for all simulations, and we saved atomic coordinates by every 1 ps for the trajectory analysis. The force field parameters of MXene and the arsenous acid were adapted from previous literature [50,51] where the atomic charge of the arsenous acid was obtained using the ESP method with the B3LYP/6-31G*(3df,3pd) basis set after geometry optimization with the B3LYP/6-31G* basis set. We used NAMD2 [52,53] for all MD simulations and VMD [54] for all the graphics shown in this report.

3. Results and discussion

3.1. Adsorbent characterization

The powder X-ray diffractograms of the stacked and un-stacked MXenes are depicted in Fig. 3. The peaks at 6.6°, 9°, 19°, and 38° for the stacked MXenes correspond to Ti_3AlC_2. After exfoliation, the peak at 6.6° gets broader and the peaks at 9° and 38° fade due to the formation of TiO_2 nanoparticles on the surface of MXenes. XRD peaks at 25.5°, 45°, 47°, and 52.5° on the stacked MXenes XRD patterns

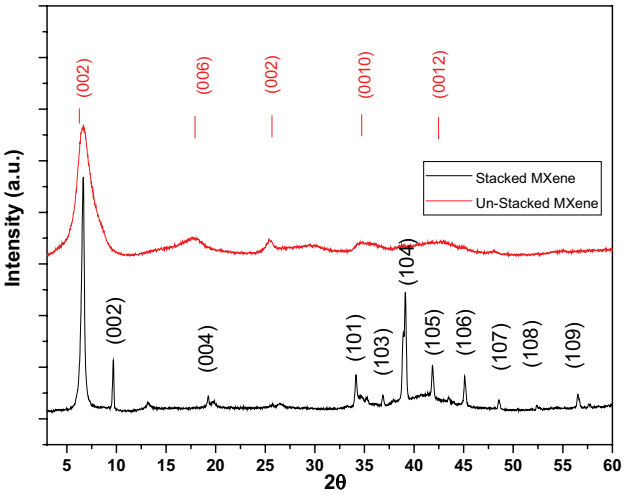

Fig. 3. XRD patterns of MXenes before (unstacked) and after exfoliation (stacked).

correspond to TiO_2 nanoparticles. Peaks at 25.5° and 45° on the un-stacked MXenes are shifted to 25° and 42.5° due to a loss of the diffraction signal in the out-of-plane direction after exfoliation that causes a broadening of the non-polar shape of the MXene nanosheets [32]. The Al impurities are also evident at 25.5°, 34°, 36°, and 41° [25].

The TGA and differential thermal analysis curves of $Ti_3C_2T_x$ are shown in Fig. 4. The thermal characteristics of $Ti_3C_2T_x$ are divided into three different stages. The first stage, which initiates from room temperature up to 200°C, is associated with the loss of H_2O, solvents, and gases such as O_2, which are physically attached to the surface of $Ti_3C_2T_x$. The weight loss corresponding to this stage is around 3%–4% of the original weight of the sample. The second stage is associated with 5% weight loss and ranges from 300°C to 650°C. The weight loss in this step is due to the loss of hydroxyl groups (–OH) from the surface of the MXenes [55,56]. The third and last stage which ranges from 650°C to 1,350°C, and corresponds to a weight loss of approximately 9%, is due to the reduction of TiO_2 to form metallic Ti [55–57].

The effect of pH on the surface charge of the MXenes was studied by zeta potential analysis. The zeta potential of MXenes, as a function of different pH values, is shown in Fig. 5. From the figure, the isoelectric point or point of zero charge is observed to be at a pH of 2.41. The positive charge maintained for the MXenes at a pH below 2.41 is attributed to the protonation of hydroxyl groups on the surface of the MXenes [22]. The zeta potential of the MXenes decreased (increase in negative sign of zeta potential) with an increase in pH, up to a pH 11. This decrease in negative charge is attributed to the increase in OH^- groups in the solution and deprotonation of the hydroxyl groups on the surface of the MXenes [58]. After pH 11, the surface charge of the MXenes increased further (decrease in negative sign of zeta potential) [25]. This sudden change in the surface charge could be due to the desorption of As ions from the surface of MXenes, which will be explained in detail in a further section. Therefore, when arsenic is desorbed from the surface of the MXenes, a less negative surface charge

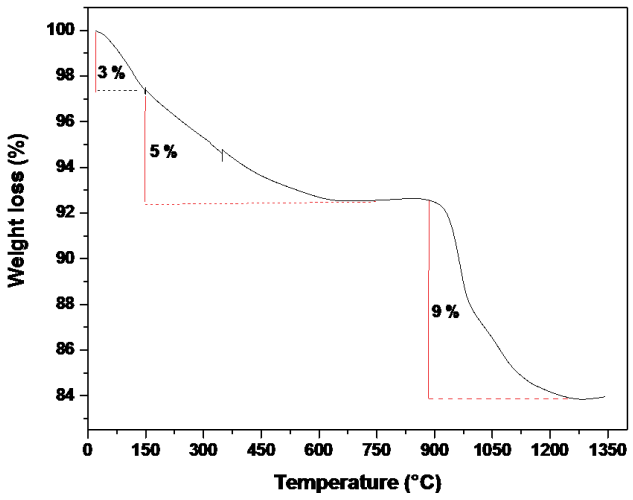

Fig. 4. TGA curve of $Ti_3C_2T_x$ from room temperature to 1,400°C under argon.

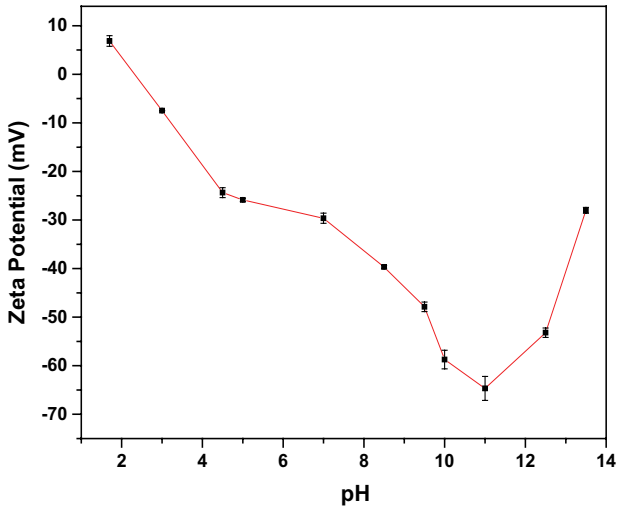

Fig. 5. Zeta potential analysis of MXene at different pH values.

is induced. When arsenic ions are adsorbed on the surface of MXenes, the electrical double layer interactions cause a heterogeneous distribution of the charges on the surface, which in turn causes reduction in the effect of the double layer repulsion during the adsorption process [59,60].

The adsorption–desorption isotherms of the stacked and un-stacked MXenes ($Ti_3C_2T_x$) are presented in Fig. 6a and follow a type IV nitrogen adsorption isotherm, exhibiting a clear hysteresis loop which represents mesoporous slit-shaped pores [61]. The slit-shaped pores are formed due to the multi-layer 2D parallel structure of $Ti_3C_2T_x$, signifying the mesoporous nature of the MXenes. The specific surface area of the delaminated MXenes increases sharply from 3.5 to 13 m^2/g after sonication, due to the unstacking of MXene layers. Fig. 6b presents the Barrett–Joyner–Halenda (BJH) isotherm and provides the pore size distribution of the stacked and un-stacked MXenes. The average pore diameter of MXenes, determined from Fig. 6b, ranges between 10 and 220 nm with a majority lying in the range of 100 nm. Unstacking of the MXene layers enhances the surface area which provides extra active sites for the adsorption of arsenic ions. The stacking of MXenes did not significantly improve their pore size distribution as shown in Fig. 6b (inset).

The SEM images in Fig. 7 show the exfoliated MXene nanosheets. As seen in Fig. 7a through Fig. 7c, the MXenes contain very few lamellar grains with densely aligned nanosheet-like structures. Etching away and delaminating the Al layer through exfoliation resulted in the presence of a gap between MXene layers which is reported to be around 6–8 Å to produce a book-like layered structure as shown in Fig. 7d [30,57,62–64]. As stated in the literature, the gap distances vary depending on the extent of exfoliation and the type of acid used to exfoliate the MAX

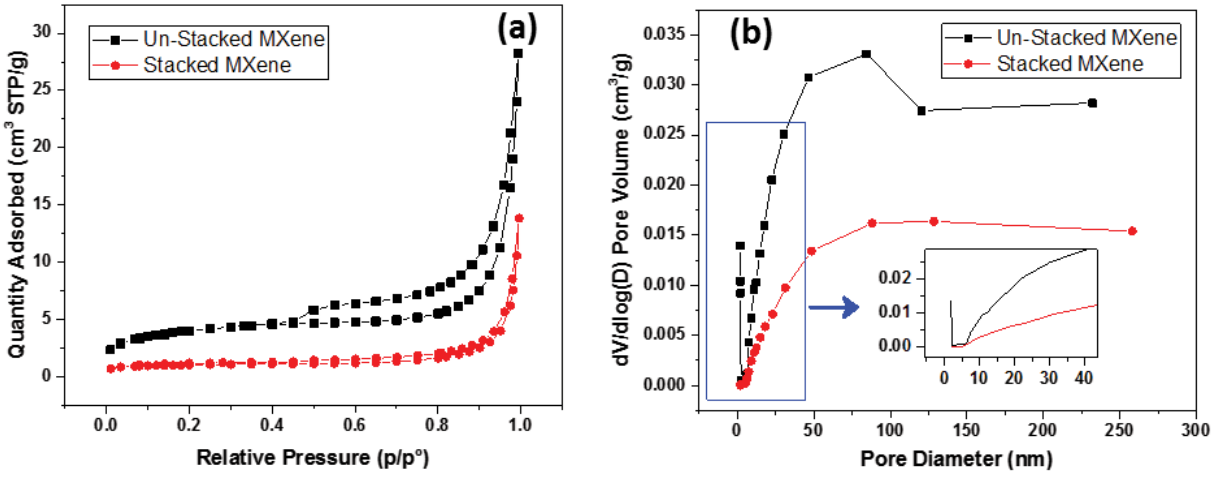

Fig. 6. Adsorption–desorption isotherms of stacked and un-stacked MXene using N_2 at 77 K (a) and pore size distribution using BJH method stacked (b).

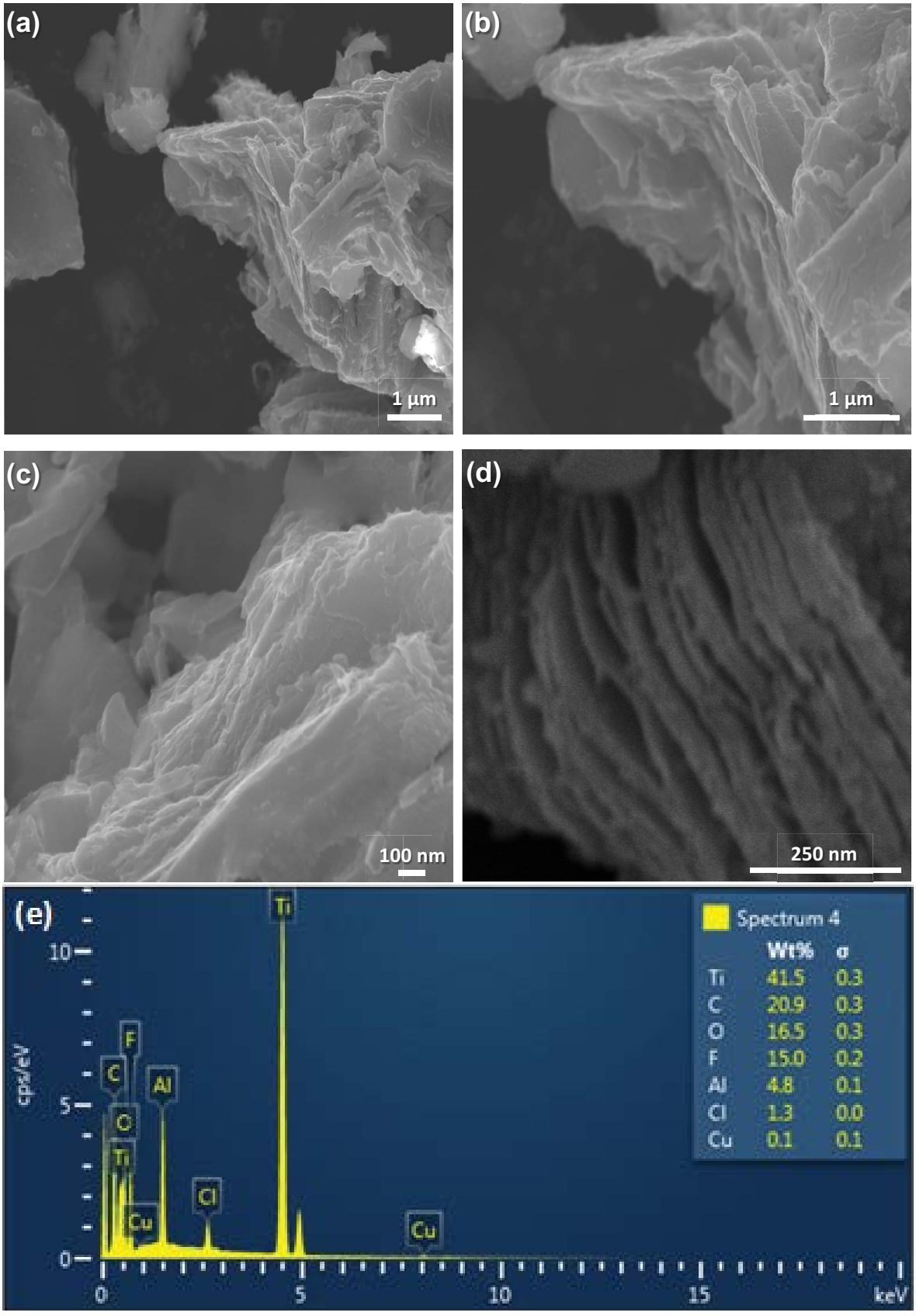

Fig. 7. SEM images of MXene after HF treatment (a–d) and EDS elemental analysis of the surface of the MXene sample (e).

phase [57,63,64]. The thickness of the MXene layer that could be estimated by the SEM image in Fig. 7d was found to be 40–50 nm [60]. SEM-EDS elemental analysis as shown in Fig. 7e reveal that the MXenes were primarily composed of Ti (41.5 wt.%) and C (~21 wt.%) and some impurities of F, Al and Cl formed during the exfoliation and de-stacking process.

From the SEM images, balls and grains can be observed on the surface of the MXenes and more notably on the edges of the MXene layers. Dall'Agnese et al. [65] attributed the spherical particles on the outer surface of the MXenes to mixed carboxides (TiC_xO_y) and TiO_2 nanoparticles formed by the oxidation of Ti present in the structure of MXenes. On the other hand, Li et al. [57] attributed the spherical particles to Ti_3C_2 and AlF_3 nanoparticles formed during the exfoliation process. It is likely that the AlF_3 nanoparticles nucleated and grew from the HF solution according to the chemical reaction in Eq. (16).

$$Ti_3AlC_2(s) + 3HF(l) \rightarrow Ti_3C_2(s) + AlF_3(s) + \frac{3}{2}H_2(g) \quad (16)$$

According to Eq. (16), the Ti_3C_2 and AlF_3 products exist in a 1:1 molar ratio, therefore, both TiO_2 and AlF_3 could be present on the surface of MXene [57].

To better understand the chemical composition of the spherical structures on the surface of MXenes, SEM (Figs. 8a and b) and EDS (Fig. 8c) characterizations were performed on the spherical particles. Around 70 wt.% of the area where the EDS was conducted was observed to be Ti and O which reveal their correspondence to TiO_2 nanoparticles and are believed to be formed by the oxidation of Ti in the MXene structures. The presence of other impurities (Al, F, Cl) could arise from the by-products of the exfoliation process.

STEM/EDS chemical mapping (Fig. 9) reveals the homogenous distribution of oxygen and arsenic species of the dried MXenes after As(III) adsorption test. As(III) and O mapping (Fig. 9d) depicts that O and As(III) are localized in the same area indicating the role of the hydroxyl groups on arsenic adsorption. Comparing Figs. 9b and c shows that the adsorption of As ions on the regions with higher oxygen content is higher.

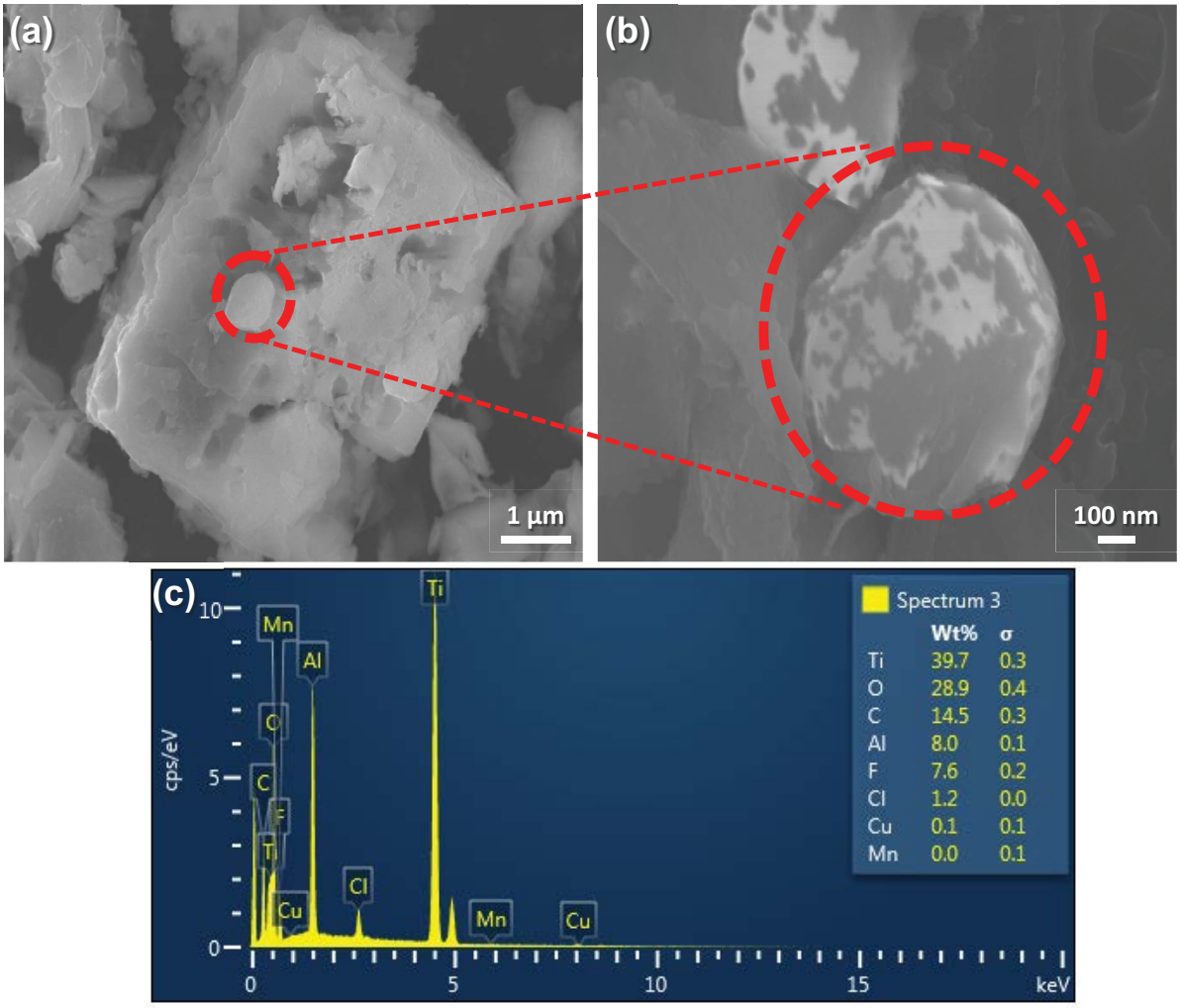

Fig. 8. SEM images of impurities on the surface of MXene (a and b) and EDS elemental analysis of the spherical particle on the surface of MXene (c).

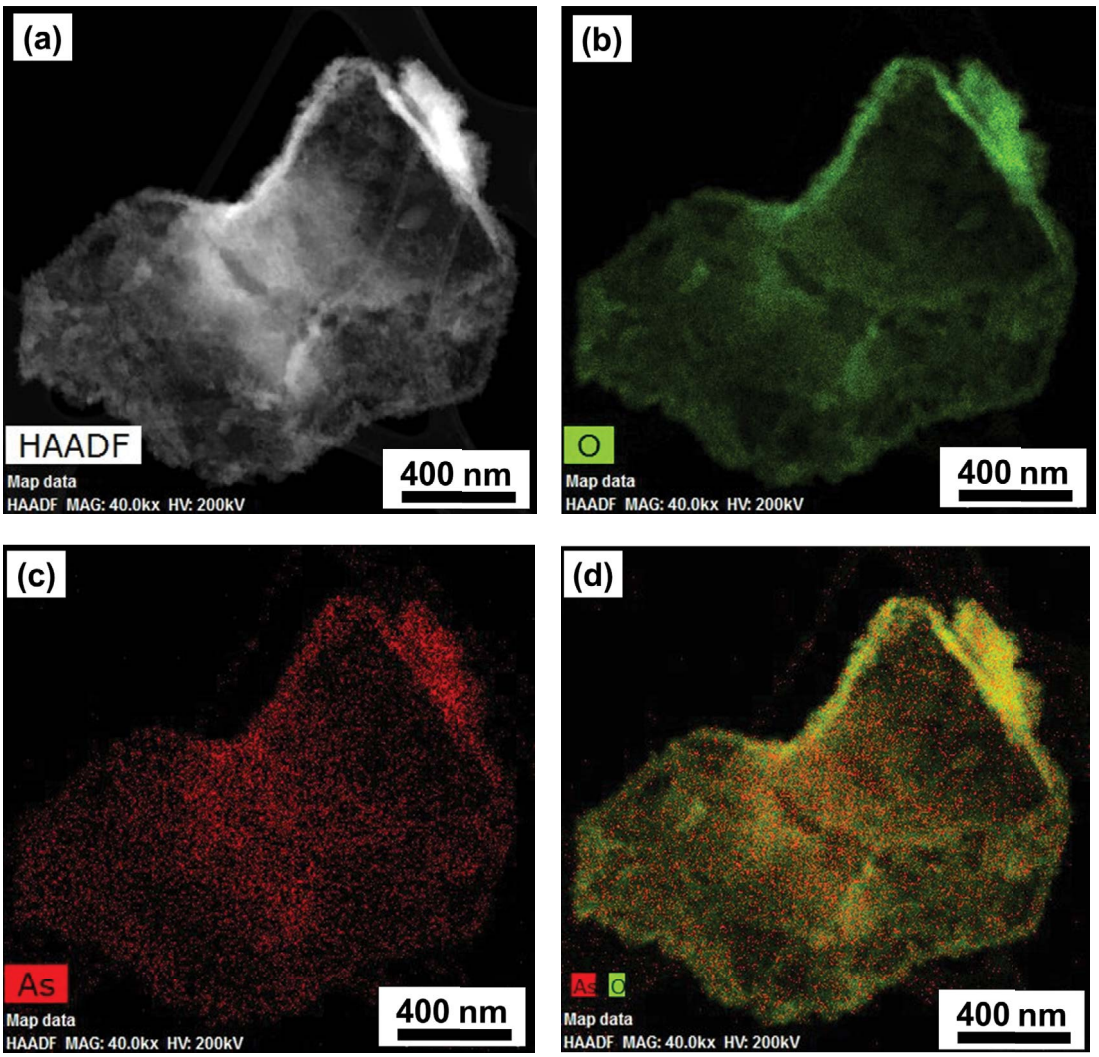

Fig. 9. STEM images of Initial status of Mxenes after adsorption: STEM image (a), O EDX map (b), As EDX map (c), As, O EDX map (d).

3.2. Adsorption mechanism

Fig. 10 demonstrates the effect of different pH values on the adsorption of arsenic by MXenes. It can be observed that arsenic adsorption is highly dependent on the pH where maximum adsorption occurs in the highly acidic pH range. From Fig. 10, adsorption of arsenic decreases with increasing solution pH where minimum adsorption is observed at a pH of 8 in this study. As seen earlier in Fig. 5, MXenes hold a positive charge below pH 2.41, after which they maintain a negative surface charge value. However, arsenic is protonated at the lower pH. Therefore, when the pH is less than 6, the anionic arsenic is dominant in water (H_3AsO_4, $HAsO_4^{2-}$ and $H_2AsO_4^-$) but in the pH range above 6, arsenic species such as $HAsO_4^{2-}$ and AsO_4^{3-} are the dominant species [2,66,67]. Therefore, at low pH, positively charged MXene can attract more negatively charged arsenic species and this is evident in Fig. 6. As reported by Hu et al. [66] in the pH range of 2–3, H_3AsO_4 and $H_2AsO_4^-$ are the dominant arsenic species while as the pH increases to 6, $H_2AsO_4^-$ and $HAsO_4^{2-}$ are the main arsenic species in water. At higher basic pH, arsenic species such as $HAsO_4^{2-}$ and AsO_4^{3-} are the dominant species. Therefore at pH less than pH_{ZPC} (2.41), the surface of MXene is positively charged and tends to attract negatively charged arsenic species [68,69]. On the other hand, when the pH goes above the pH_{ZPC}, the hydroxyl group on the surface of MXene gets deprotonated and become negatively charged. This change in the charge causes less adsorption for the arsenic species in water as indicated in Fig. 10. The figure depicts that the final arsenic concentration decreases with increasing adsorbent dosage.

The variations of the surface charge induced by the change in pH could be usefully utilized for MXene regeneration. In this work, to regenerate MXene, the spent MXene is washed with 0.1 M NaOH at pH above 11 and then it is washed with Di ionized water (DI) water four to five times. The powder is then centrifuged and the supernatant is freeze-dried and reused. The adsorption capacity of MXene remained unchanged after three regeneration cycles.

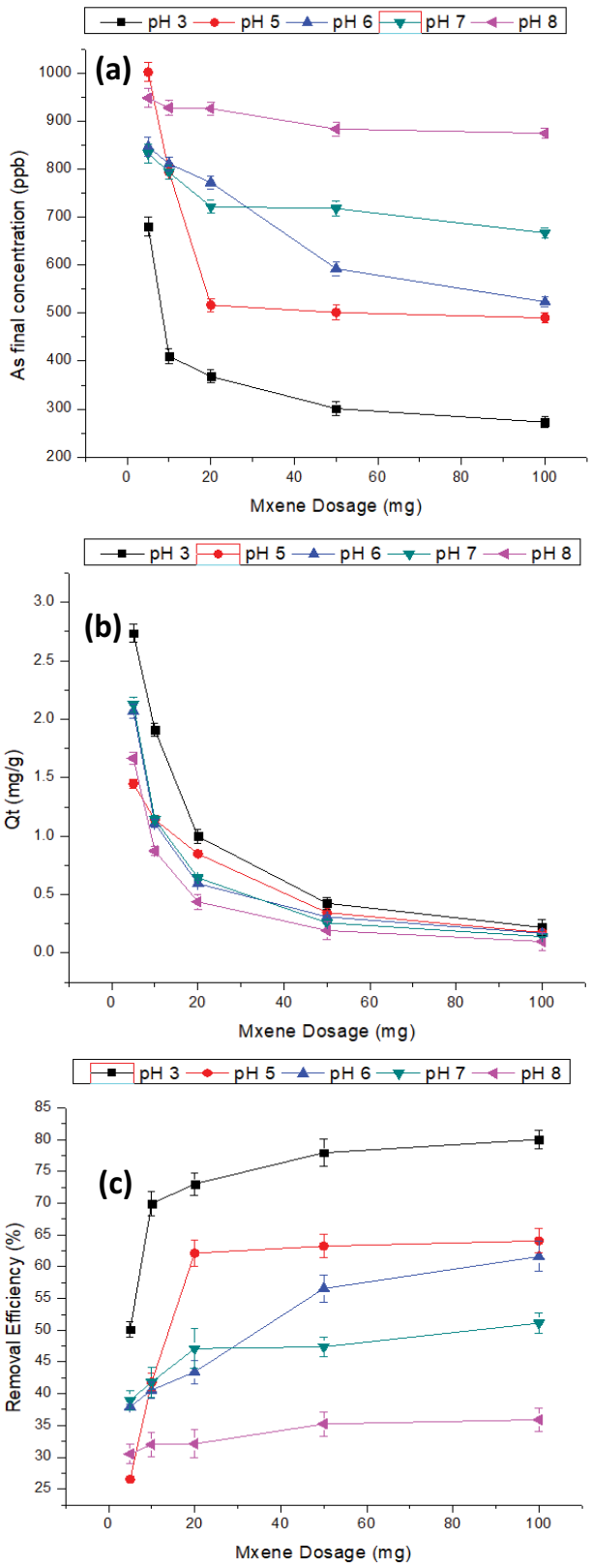

Fig. 10. Final concentration as function of adsorbent dose (a) adsorption capacity (b) and removal efficiency (c) of arsenic using MXene at different pH (temperature is kept constant at 23°C and shaking speed of 400 rpm).

MXene dosage is another important factor, which plays a major role in the arsenic uptake and can control the capacity of MXene at a given concentration. As shown in Fig. 10c, the removal efficiency of arsenic by MXene increases with increasing adsorbent dosage. The maximum removal efficiency was found to be at pH 3 with 100 mg of MXene. As a general rule, as the amount of adsorbent increases, the free adsorption sites on the surface of adsorbent available for the removal of contaminants increases proportionally. Moreover, in the case of MXene, after the exfoliation process by HF, MXene's surface is terminated mainly by OH, F, and O groups [21,30,62,70]. These functional groups along with the free adsorption sites on the surface of MXene provide environments for ions to be adsorbed freely on the surface of MXene either by chemical bonding between functional groups on the surface of MXene and the ions (chemisorption) or physically by van der Waals forces (physisorption). The chemical bonding between arsenic ions and functional groups was illustrated earlier in the XPS analysis as shown in Fig. 10.

As shown in the SEM images in Fig. 3, the sheet-like structure of MXene helps ions to be adsorbed within the sheet through an intercalation process. This could be the second adsorption route where arsenic is adsorbed by MXene and is sandwiched between the unstacked MXene layers. As stated in the literature [57,64] and by the results presented in the XPS analysis, the 002 peak of MXene shifts to a lower angle and becomes broader causing an increase in the *d*-spacing between the MXene sheets. The etching process results in decreasing the thickness of the MXene sheets and consequently increases the interlayer distance between each MXene layer [25,57,64]. As stated in our previous work [25], the interlayer distance between each MXene sheet is estimated to be in the range of 7–20 Angstrom depending on the extent of exfoliation and the type of acid used to exfoliate the MAX phase [57,63,64]. Comparing the atomic radii of arsenic which is around 114 pm to the inter-layer distance between MXene sheets, one can conclude that some of the arsenic ions are intercalated within the MXene layers either chemically or physically.

The third and last possible route for arsenic adsorption is through ion-exchange process. The presence of functional groups such as –OH and –F may act as a capturing site for arsenic adsorption by an ion exchange reaction. This was evident in the XPS analysis where As was captured by functional groups such as –OH and –F groups. The arsenic will be attracted to the functional groups and undergo ion exchange. These groups are mostly negatively charged forming Ti–As and O–As bonding. This has been previously explained by the XPS analysis too.

In this work, the value of adsorption capacity of arsenic removal was found to be higher compared with the adsorption capacities for different adsorbents reported in literature (Table 1).

3.3. Effect of contact time and adsorption kinetics

Kinetic experiments were carried out by determining the solution As(III) contents at various time intervals. The contact time was varied from 0 to 2 h using 100 mg of MXene with an initial As(III) concentration of 1.4 mg/L

Table 1
Sorption capacities for arsenic removal of different adsorbents

Adsorbent	Sorption capacity (mg/g)	Reference
Multiwall carbon nanotube–zirconia nanohybrid	2	[75]
Coal-based mesoporous activated carbon	1.634	[76]
TiO_2, $Ti(OH)_4$ and sulfated TiO_2	0.2543, 0.2625 and 0.3425	[77]
Chitosan/chitin mixture	0.2543	[78]
Copper(II) oxide	1.0862	[79]
Carbon cryogel/ceria nanocomposite	2.5	[80]
Aluminum hydroxide (gibbsite)	0.5904	[81]
Iron oxide–coated cement	0.67	[82]
Activated alumina	0.23	[13]
Iron oxide–coated sand	0.02857	[12]
Iron-treated activated carbon	0.01573	[83]
Iron oxide–coated granular activated charcoal	0.0012	[84]
MXene	2.75	This study

(1.4 ppm) (shaking at 400 rpm). Fig. 11 shows the effect of contact time at different pH values.

More than 80% of As(III) was removed after 2 h of contact time at a pH of 3. The adsorption processes for As(III) were rapid within the first 10 min, and reached equilibrium within about 2 h. In contrast, activated carbon requires a few hours of contact time to remove a similar percentage of removal of arsenic [81]. This rapid kinetics is mainly endorsed to the distinctive layered nanostructure of MXene, which favors for the accessibility of As(III) for intercalation and diffusion. In general, MXene showed excellent kinetics where almost 40% of As(III) was removed just after dosing. The high removal efficiency rate at the beginning of the contact time was due to the large number of vacant binding sites available for the adsorption of arsenic ions. As the outside surface of MXene becomes exhausted and saturated with arsenic ions, the uptake rate of arsenic by MXene decreases and reaches equilibrium. The rapid removal rate suggests that the adsorption processes apparently included two stages, namely, electrostatic attraction and surface complexation or ion-exchange between arsenic and MXene as described earlier.

The rate and the kinetics of As uptake by MXene were investigated using two common models, namely, the Lagergren pseudo-first-order model and pseudo-second-order model at different pH values. The arsenic adsorption data with MXene fit very well to the pseudo-second-order model with a coefficient of determination being close to unity. The data do not show a linear behavior in the first-order model and therefore the system cannot be correlated to the first-order kinetic model. The R^2 of the linearized plots for the first-order model are less than 0.5 for all cases. Fig. 12 illustrates the pseudo-second-order model fitting for the As(III) adsorption and the constants are summarized in Table 2. It is clear from Fig. 12 that the adsorption rate increases with increasing pH and the highest adsorption capacity occurs at pH 3. Also, it can be concluded that the adsorption of As at pH 3 is very rapid with most of the adsorption occurring within the first 20–30 min. From Table 1, the calculated experimental Q_e

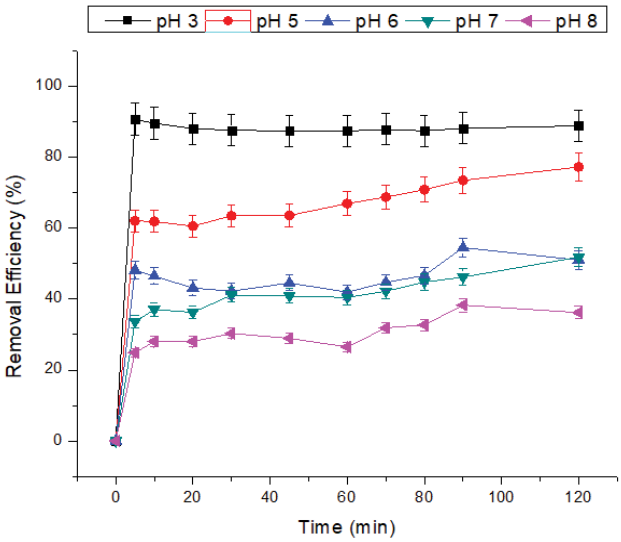

Fig. 11. Effect of contact time on removal of As(III) by MXene at different pH (temperature is kept constant at 23°C and shaking speed of 400 rpm).

and theoretical Q_e values have excellent agreement; thus, a pseudo-second-order model can be assumed to be the rate-limiting step and the adsorption process is driven by chemical sorption between the adsorbate and adsorbent.

Both the calculated and experimental Q_e values for As(III) adsorption were close to each other. Therefore, the high correlation coefficient and the agreement between experimental and calculated Q_e values both suggest that the overall adsorption kinetics of As(III) on MXene followed the pseudo-second-order model and interacted through a chemisorption process.

3.4. Adsorption isotherm analysis

The adsorption isotherm models of Langmuir, Freundlich, and D-R were applied to fit the adsorption equilibrium

Table 2
Kinetic parameters for the second-order model

pH	Q_e (mg/g)	k_2 (g/mgh)	R^2
3	0.241	25.38	0.99
5	0.207	1.18	0.99
6	0.139	2.008	0.98
7	0.135	1.282	0.99
8	0.099	0.0177	0.99

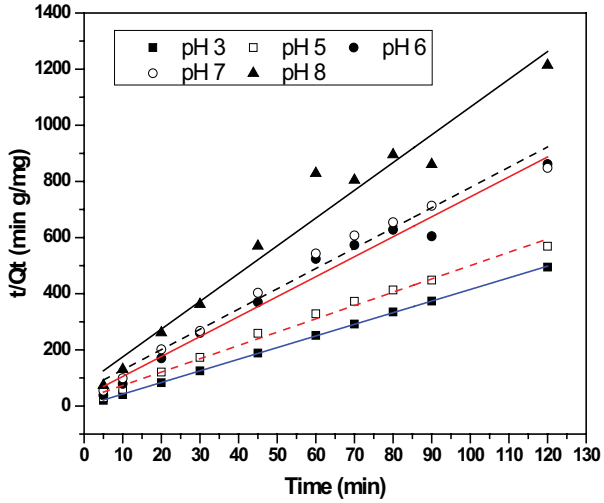

Fig. 12. Pseudo-second-order kinetic model of As uptake using MXene at different pH (temperature is kept constant at 23°C and shaking speed of 400 rpm).

data of As(III) on the MXene. Aqueous solutions with initial As(III) concentrations of 0.1, 0.4, 0.8, 1, and 3 mg L^{-1} were used for the experiments at pH 3.0, adsorption time of 2 h, and temperature of 25°C. The adsorption isotherms were simulated with the previously mentioned models (Fig. 13) and the constant values of the parameters calculated for each isotherm models are listed in Table 3.

The Freundlich constant $1/n$ was found to be 3.38 ($1/n > 1$), which means that the As(III) adsorption on MXene surface is a very favorable process. At room temperature (25°C), the Freundlich model fitted the adsorption isotherm better than the Langmuir model ($R^2 = 0.75$) for As(III). This means that As(III) adsorption is not a single-site monolayer adsorption process. The XPS analysis confirmed the presence of a number of surfaces bond types and adsorbed species. The Freundlich isotherm is more widely used, but it does not provide any information on the monolayer adsorption capacity in contrast to the Langmuir model. The Freundlich isotherm describes the adsorption process as not being restricted to the formation of a monolayer and As(III) ions are adsorbed onto the heterogeneous surface of MXene. Therefore, the amount of As(III) adsorbed on MXene is the summation of the adsorption on all sites (each having its own bond energy), with the stronger binding sites occupied first, until the adsorption energy exponentially decreases upon the completion of the adsorption process.

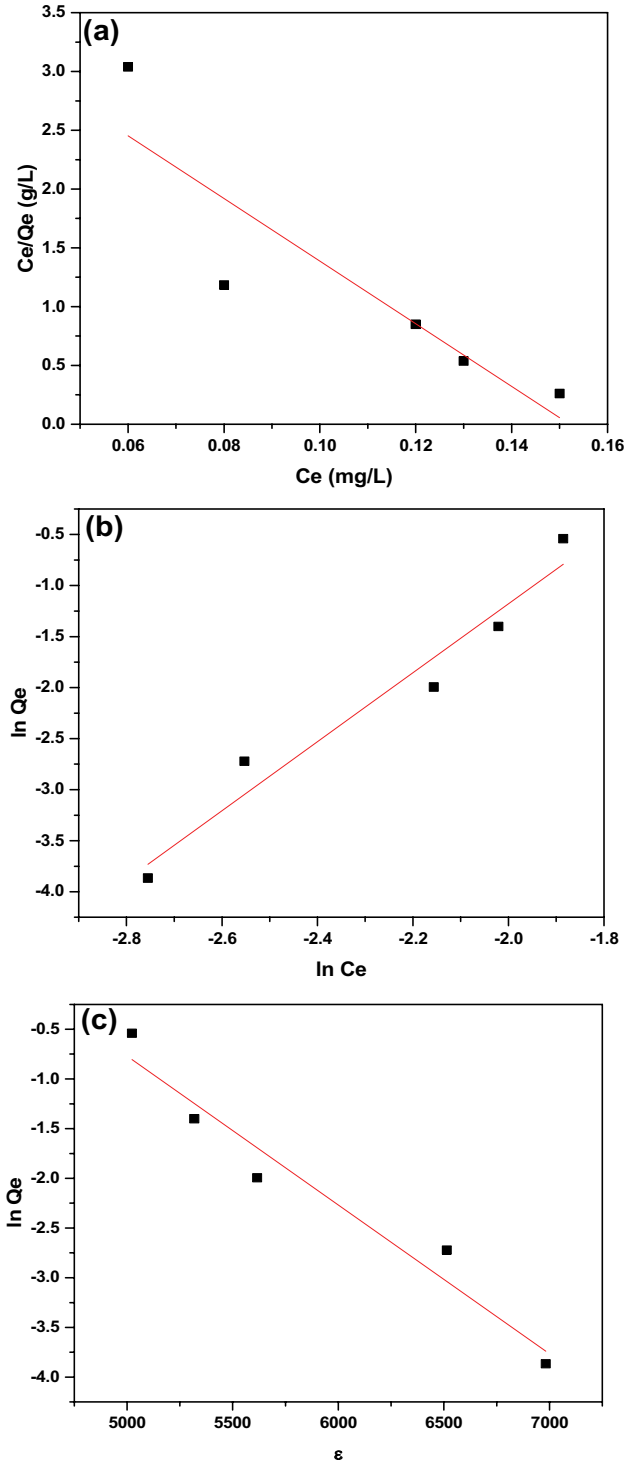

Fig. 13. (a) Langmuir, (b) Freundlich, and (c) D-R adsorption isotherms of As(III) on the MXene (temperature is kept constant at 23°C and shaking speed of 400 rpm).

The mean free energy (E) of the adsorption process between As(III) and MXene is found using the D-R isotherm (Fig. 14). The E (kJ/mol) value presents information about the adsorption mechanism, which is physical or chemical, and can be obtained from the D-R model. If the value

Table 3
Langmuir, Freundlich, and D-R parameters for adsorption isotherm of As(III) on MXene at 25°C with R^2 values corresponding to linear fitting of the data

Langmuir parameters		
X_m (mg/g)	K (L/mg)	R^2
–0.037	–6.45	0.76
Freundlich parameters		
K_f (mg/g)	$1/n$	R^2
0.0038	3.38	0.95
D-R parameters		
Q_m (mg/g)	B (mol²/kJ²)	R^2
829.23	0.00075	0.93

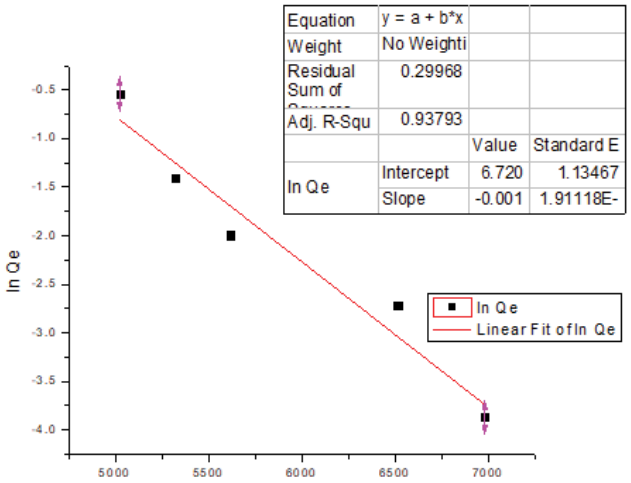

Fig. 14. D-R adsorption isotherms of barium, on the MXene.

of binding energy is between 8 and 16 kJ/mol, then the adsorption process follows chemical ion-exchange, while E < 8 kJ/mol, means the adsorption process proceeds physically, whereas if the value is more than 16 kJ/mol, the adsorption process is chemisorption in nature [82]. The mean sorption energy for As(III)–MXene interaction found from values in Table 2 was 18.51 kJ/mol. This result suggests that the majority of the adsorption of As(III) ions on the surface of MXene is a chemisorption process in agreement with the results found by XPS analysis.

As shown in Fig. 14, the global minimum energy between arsenic (arsenous acid) and the MXene surface using the SMD simulation is found to be around 7.1 kJ/mol. The value of 7.1 kJ/mol only considers the arsenic adsorption from the top surface of MXene. Considering other adsorption routes such as intercalation between the MXene layer would cause increasing the energy by two-folds. Intercalation would cause adsorption from two opposed surface to the MXene and therefore increase the binding energy to be doubled that is comparable with the value of 18.5 kJ/mol found using D-R model. The slight difference between the D-R estimated value and the SMD

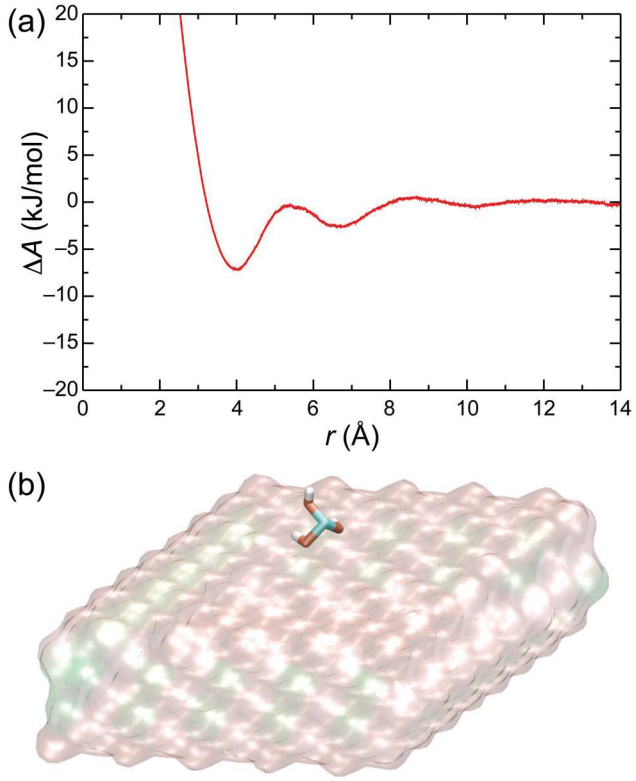

Fig. 15. (a) The free energy profile of adsorption of the arsenous acid on the surface of MXene. The global minimum energy of 7.1 kJ/mol was found at r = ~4 Å. (b) The conformation of the arsenous acid obtained when r = ~4 Å.

simulation value can be related to the assumptions used in the D-R model where the D-R model is developed for adsorption of gases and vapors by microporous solids. Furthermore, the D-R model is based on physical adsorption where most of the adsorption occurs by pore filling rather than layer-by-layer formation of films on the surface of the adsorbent such as MXene.

3.5. Interference studies

To challenge the adsorption of arsenic by MXene, a solution containing As(III), Pb(II), Cr(IV), Sr(II), and Ba(II) with 1 ppm concentration was prepared. The MXene performance is tested under batch mode and the removal efficiency of MXene for each ion is reported in Fig. 16. Generally, the presence of multiple contaminations in the water creates adsorption competition and displacement between the adsorbates in the water and the adsorbent. Therefore, different ions tend to occupy the active adsorption sites on the surface of MXene based on their selectivity and electrochemical potential of the material. By designing such experiments, the affinity of different ions under consideration can be examined. As illustrated in Fig. 16, arsenic removal was reduced only very slightly in the system of multi ions (77%) compared with the system where only arsenic ions are present (88%). For other coexisting metal ions, the uptake of

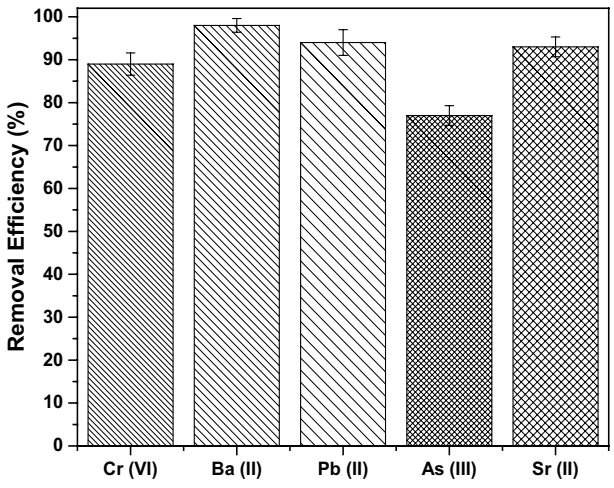

Fig. 16. Adsorption performances of various metal uptakes on MXene in a multiple-metal solution (temperature is kept constant at 23°C and shaking speed of 400 rpm).

Ba(II) was around 98%, while Pb(II), Sr(II), and Ca(II) ions were removed by about 94%. The results in Fig. 16 showed that ions with 2 cationic charges have more affinity for being adsorbed by MXene compared with 3 or 5 cationic charges [25]. Ba(II) was the dominant competing ion, whose species is very similar to the Pb(II) and Sr(II) and which have also been studied by Peng et al. [21].

The distribution coefficient (K_D) can be used as a mathematical indication to demonstrate the selectivity and affinity of an ion towards an adsorbent. The distribution coefficient (K_D) is calculated as [83]:

$$K_D = \frac{\left(C_i - C_e\right)}{C_e}\left(\frac{V}{m}\right) \tag{17}$$

where C_i and C_e are initial and equilibrium concentrations, V is the volume of solution, and m is the mass of adsorbent. The calculated distribution coefficient was in the following order: Ba > Sr > Ca > Pb > Cr >> As with K_D values of 68.0, 64.3, 63.9, 61.5, 36.0, and 3.6 mg/mL, respectively [25].

As indicated earlier in Fig. 7, the MXene surface in the pH range above 2.41 is negatively charged, therefore ions with a higher electronegativity are adsorbed more by MXene compared with those with lower electronegativity. The electronegativities of As, Cr, Pb, Sr, and Ba are 2.20, 1.56, 1.55, 0.99, and 1.04, respectively (As > Cr > Pb > Sr > Ba). Comparing the electronegativity values with the adsorption removal efficiencies in Fig. 10, the affinity of MXene to remove the multiple ions is in the order of Ba > Sr > Pb > Cr > As. Although as per the electronegativity values, the adsorption of arsenic should be higher but as indicated earlier and as indicated by the distribution coefficient, the affinity of MXene to adsorb ions with two cationic charge is more than ions such as As with 3 cationic charges. Another factor is the surface charge of MXene which is negative at pH 7 (i.e., mimicking drinking water) and the arsenic speciation at this pH is also negative causing electrostatic repulsion and reduction in the adsorption. The presence of functional groups such as –OH and –F groups on the surface of MXene also plays a role in attracting divalent ions compared with trivalent ions [84,85]. Quite a high arsenic adsorption in systems containing multi-ions can be a promising result, when the system under treatment contains more than one ion within a complex chemical environment.

4. Conclusion

In summary, we have successfully developed a simple and efficient method to remove the arsenic trivalent from water using titanium metal carbide MXene 2D nanosheet. The material has been characterized using SEM, EDS, XRD, XPS, BET N_2 adsorption, and TGA. In particular, MXene has only 13 m^2/g specific surface area with most of the particle ranging in the range of 100–150 nm. $Ti_3C_2T_x$ nanosheet was prepared by an intercalation and exfoliation process and showed an outstanding removal capacity for toxic As(III). The maximum removal capacity is 2.8 mg/g, which is similar to other competitors such as activated carbons and carbon nanotubes due to the high number of hydroxyl group on the surface. The removal efficiency of As(III) and residual As(III) by MXene in treated water was far below the drinking water standard limit suggested by the WHO which is 10 μg/L. The effect of pH on removal efficiency was investigated in depth and it was found that the optimum condition occurred at pH 3, which has the best As(III) removal performance. The results using SMD simulation showed that the binding energy between arsenic and MXene is to be around 7.1 kJ/mol. Based on their unique structure and chemistry such as well-dispersibility and surface area and its superior adsorption for the removal of arsenic from water, MXene nanosheets are thought to be a promising adsorption material for removal of heavy metals from wastewater and drinking water.

Acknowledgments

The authors would like to thank Dr. Yury Gogotsy and the Nano Material Group at Department of Materials Science and Engineering and the A.J. Drexel Nanomaterials Institute, Drexel University, Philadelphia for providing MXene for this study. The authors are grateful to the Qatar Environment and Energy Research Institute (QEERI), Qatar Foundation, for the financial support. Authors also would like to thank Mohammad Hilal for conducting SEM imaging and Adnan Ali at QEERI for his helpful discussions and technical assistance. Also the authors are grateful to the Center of Advanced Material (CAM) at Qatar University for facilitating zeta potential analysis.

References

[1] WHO, Guidelines for Drinking-Water Quality, Geneva, 2008.
[2] D. Mohan, C.U. Pittman Jr., Arsenic removal from water/wastewater using adsorbents—a critical review, J. Hazard. Mater., 142 (2007) 1–53.
[3] A.V. Vitela-Rodriguez, J.R. Rangel-Mendez, Arsenic removal by modified activated carbons with iron hydro(oxide) nanoparticles, J. Environ. Manage., 114 (2013) 225–231.

[4] W.-G. Li, X.-J. Gong, K. Wang, X.-R. Zhang, W.-B. Fan, Adsorption characteristics of arsenic from micro-polluted water by an innovative coal-based mesoporous activated carbon, Bioresour. Technol., 165 (2014) 166–173.
[5] R. Sandoval, A.M. Cooper, K. Aymar, A. Jain, K. Hristovski, Removal of arsenic and methylene blue from water by granular activated carbon media impregnated with zirconium dioxide nanoparticles, J. Hazard. Mater., 193 (2011) 296–303.
[6] M. Zhang, B. Gao, S. Varnoosfaderani, A. Hebard, Y. Yao, M. Inyang, Preparation and characterization of a novel magnetic biochar for arsenic removal, Bioresour. Technol., 130 (2013) 457–462.
[7] D.M. Sherman, S.R. Randall, Surface complexation of arsenic(V) to iron(III) (hydr)oxides: structural mechanism from ab initio molecular geometries and EXAFS spectroscopy, GCA, 67 (2003) 4223–4230.
[8] K.Y. Foo, B.H. Hameed, Mesoporous activated carbon from wood sawdust by K_2CO_3 activation using microwave heating. Bioresour. Technol., 111 (2012) 425–432.
[9] K. Kadirvelu, M. Kavipriya, C. Karthika, M. Radhika, N. Vennilamani, S. Pattabhi, Utilization of various agricultural wastes for activated carbon preparation and application for the removal of dyes and metal ions from aqueous solutions, Bioresour. Technol., 87 (2003) 129–132.
[10] K. Lizama Allende, T.D. Fletcher, G. Sun, The effect of substrate media on the removal of arsenic, boron and iron from an acidic wastewater in planted column reactors, Chem. Eng. J., 179 (2012) 119–130.
[11] V.K. Gupta, V.K. Saini, N. Jain, Adsorption of As(III) from aqueous solutions by iron oxide-coated sand, J. Colloid Interface Sci., 288 (2005) 55–60.
[12] T.S. Singh, K.K. Pant, Equilibrium, kinetics and thermodynamic studies for adsorption of As(III) on activated alumina, Sep. Purif. Technol., 36 (2004) 139–147.
[13] M.S. Onyango, Y. Kojima, Y. Kojima, H. Matsuda, H. Matsuda, A. Ochieng, A. Ochieng, Adsorption kinetics of arsenic removal from groundwater by iron-modified zeolite, J. Chem. Eng., 12 (2003) 1516–1522.
[14] S.-L. Lo, H.-T. Jeng, C.-H. Lai, Characteristics and adsorption properties of iron-coated sand, Water Sci. Technol., 35 (1997) 63–70.
[15] C.A.J. Appelo, M.J.J. Van Der Weiden, C. Tournassat, L. Charlet, Surface complexation of ferrous iron and carbonate on ferrihydrite and the mobilization of arsenic, Environ. Sci. Technol., 36 (2002) 3096–3103.
[16] S. Fendorf, M.J. Eick, P. Grossl, D.L. Sparks, Arsenate and chromate retention mechanisms on goethite. 1. Surface structure, Environ. Sci. Technol., 31 (1997) 315–320.
[17] K.P. Raven, A. Jain, R.H. Loeppert, Arsenite and arsenate adsorption on ferrihydrite: kinetics, equilibrium, and adsorption envelopes, Environ. Sci. Technol., 32 (1998) 344–349.
[18] W. Driehaus, M. Jekel, U. Hildebrandt, Granular ferric hydroxide—a new adsorbent for the removal of arsenic from natural water, J. Water Supply Res. Technol., 47 (1998) 30–35.
[19] Y. Xu, L. Axe, Synthesis and characterization of iron oxide-coated silica and its effect on metal adsorption, J. Colloid Interface Sci., 282 (2005) 11–19.
[20] J.A. Muñoz, A. Gonzalo, M. Valiente, Arsenic Adsorption by Fe(III)-loaded open-celled cellulose sponge. Thermodynamic and selectivity aspects, Environ. Sci. Technol., 36 (2002) 3405–3411.
[21] Q. Peng, J. Guo, Q. Zhang, J. Xiang, B. Liu, A. Zhou, R. Liu, Y. Tian, Unique lead adsorption behavior of activated hydroxyl group in two-dimensional titanium carbide, J. Am. Chem. Soc., 136 (2014) 4113–4116.
[22] Y. Ying, Y. Liu, X. Wang, Y. Mao, W. Cao, P. Hu, X. Peng, Two-dimensional titanium carbide for efficiently reductive removal of highly toxic chromium(VI) from water, ACS Appl. Mater. Interfaces, 7 (2015) 1795–1803.
[23] M. Xu, T. Liang, M. Shi, H. Chen, Graphene-like two-dimensional materials, Chem. Rev., 113 (2013) 3766–3798.
[24] K.S. Novoselov, A.K. Geim, S.V. Morozov, D. Jiang, Y. Zhang, S.V. Dubonos, I.V. Grigorieva, A.A. Firsov, Electric field effect in atomically thin carbon films, J. Sci., 306 (2004) 666–669.
[25] A.K. Fard, G. Mckay, R. Chamoun, T. Rhadfi, H. Preud'Homme, M.A. Atieh, Barium removal from synthetic natural and produced water using MXene as two dimensional (2-D) nanosheet adsorbent, Chem. Eng. J., 317 (2017) 331–342.
[26] L. Wang, L. Yuan, K. Chen, Y. Zhang, Q. Deng, S. Du, Q. Huang, L. Zheng, J. Zhang, Z. Chai, Loading actinides in multilayered structures for nuclear waste treatment: the first case study of uranium capture with vanadium carbide MXene, ACS Appl. Mater. Interfaces, 8 (2016) 16396–16403.
[27] Y. Wu, H. Pang, Y. Liu, X. Wang, S. Yu, D. Fu, J. Chen, X. Wang, Environmental remediation of heavy metal ions by novel-nanomaterials: a review, Environ. Pollut., 246 (2019) 608–620.
[28] K. Rasool, R.P. Pandey, P.A. Rasheed, S. Buczek, Y. Gogotsi, K.A. Mahmoud, Water treatment and environmental remediation applications of two-dimensional metal carbides (MXenes), Appl. Mater. Today, 30 (2019) 80–102.
[29] I. Ihsanullah, MXenes (two-dimensional metal carbides) as emerging nanomaterials for water purification: progress, challenges and prospects, Chem. Eng. J., 388 (2020) 124340.
[30] M. Naguib, M. Kurtoglu, V. Presser, J. Lu, J. Niu, M. Heon, L. Hultman, Y. Gogotsi, M.W. Barsoum, Two-dimensional nanocrystals produced by exfoliation of Ti_3AlC_2, Adv. Mater., 23 (2011) 4248–4253.
[31] R. Sheha, E. Metwally, Equilibrium isotherm modeling of cesium adsorption onto magnetic materials, J. Hazard. Mater., 143 (2007) 354–361.
[32] A. Günay, E. Arslankaya, I. Tosun, Lead removal from aqueous solution by natural and pretreated clinoptilolite: adsorption equilibrium and kinetics, J. Hazard. Mater., 146 (2007) 362–371.
[33] H. Yuh-Shan, Citation review of Lagergren kinetic rate equation on adsorption reactions, Scientometrics, 59 (2004) 171–177.
[34] Y.-S. Ho, G. McKay, Pseudo-second order model for sorption processes, Process Biochem., 34 (1999) 451–465.
[35] P. Mark, L. Nilsson, Structure and dynamics of the TIP3P, SPC, and SPC/E water models at 298 K, J. Phys. Chem. A, 105 (2001) 9954–9960.
[36] O.S. Lee, M.A. Carignano, Exfoliation of electrolyte-intercalated graphene: molecular dynamics simulation study, J. Phys. Chem., 119 (2015) 19415–19422.
[37] S. Park, F. Khalili-Araghi, E. Tajkhorshid, K. Schulten, Free energy calculation from steered molecular dynamics simulations using Jarzynski's equality, J. Chem. Phys., 119 (2003) 3559–3566.
[38] S. Park, K. Schulten, Calculating potentials of mean force from steered molecular dynamics simulations, J. Chem. Phys., 120 (2004) 5946–5961.
[39] T. Yu, O.S. Lee, G.C. Schatz, Steered molecular dynamics studies of the potential of mean force for peptide amphiphile self-assembly into cylindrical nanofibers, J. Phys. Chem. A, 117 (2013) 7453–7460.
[40] M. Arrar, F.M. Boubeta, M.E. Szretter, M. Sued, L. Boechi, D. Rodriguez, On the accurate estimation of free energies using the jarzynski equality, J. Comput. Chem., 40 (2019) 688–696.
[41] F.M. Boubeta, R.M. Contestín García, E.N. Lorenzo, L. Boechi, D. Estrin, M. Sued, M. Arrar, Lessons learned about steered molecular dynamics simulations and free energy calculations, Chem. Biol. Drug Des., 93 (2019) 1129–1138.
[42] O.-S. Lee, Dynamic properties of water confined in graphene-based membrane: a classical molecular dynamics simulation study, Membranes, 9 (2019) 165.
[43] C. Pangali, M. Rao, B.J. Berne, Monte-Carlo simulation of the hydrophobic interaction, J. Chem. Phys., 71 (1979) 2975–2981.
[44] C. Jarzynski, Nonequilibrium equality for free energy differences, Phys. Rev. Lett., 78 (1997) 2690–2693.
[45] C. Jarzynski, Equilibrium free-energy differences from nonequilibrium measurements: a master-equation approach, Phys. Rev. E, 56 (1997) 5018–5035.
[46] G.J. Martyna, D.J. Tobias, M.L. Klein, Constant-pressure molecular-dynamics algorithms, J. Chem. Phys., 101 (1994) 4177–4189.
[47] S.E. Feller, Y.H. Zhang, R.W. Pastor, B.R. Brooks, Constant-pressure molecular-dynamics simulation - the Langevin piston method, J. Chem. Phys., 103 (1995) 4613–4621.

[48] T. Darden, D. York, L. Pedersen, Particle mesh Ewald - an *n*.Log(*n*) method for Ewald sums in large systems, J. Chem. Phys., 98 (1993) 10089–10092.
[49] S. Miyamoto, P.A. Kollman, Settle-an analytical version of the shake and rattle algorithm for rigid water models, J. Comput. Chem., 13 (1992) 952–962.
[50] H.H.G. Tsai, J.B. Lee, J.M. Huang, R. Juwita, A molecular dynamics study of the structural and dynamical properties of putative arsenic substituted lipid bilayers, Int. J. Mol. Sci., 14 (2013) 7702–7715.
[51] K. Xu, X. Ji, B. Zhang, C. Chen, Y.J. Ruan, L. Miao, J.J. Jiang, Charging/discharging dynamics in two-dimensional titanium carbide (MXene) slit nanopore: insights from molecular dynamic study, Electrochim. Acta, 196 (2016) 75–83.
[52] L. Kale, R. Skeel, M. Bhandarkar, R. Brunner, A. Gursoy, N. Krawetz, J. Phillips, A. Shinozaki, K. Varadarajan, K. Schulten, NAMD2: Greater scalability for parallel molecular dynamics, J. Comput. Phys., 151 (1999) 283–312.
[53] J.C. Phillips, R. Braun, W. Wang, J. Gumbart, E. Tajkhorshid, E. Villa, C. Chipot, R.D. Skeel, L. Kale, K. Schulten, Scalable molecular dynamics with NAMD, J. Comput. Chem., 26 (2005) 1781–1802.
[54] W. Humphrey, A. Dalke, K. Schulten, VMD: visual molecular dynamics, J. Mol. Graphics, 14 (1996) 33–38.
[55] A. Feng, Y. Yu, F. Jiang, Y. Wang, L. Mi, Y. Yu, L. Song, Fabrication and thermal stability of NH_4HF_2-etched Ti_3C_2 MXene, Ceram. Int., 43 (2017) 6322–6328.
[56] K. Wang, Y. Zhou, W. Xu, D. Huang, Z. Wang, M. Hong, Fabrication and thermal stability of two-dimensional carbide Ti_3C_2 nanosheets, Ceram. Int., 42 (2016) 8419–8424.
[57] Z. Li, L. Wang, D. Sun, Y. Zhang, B. Liu, Q. Hu, A. Zhou, Synthesis and thermal stability of two-dimensional carbide MXene Ti_3C_2, Mater. Sci. Eng. B, 191 (2015) 33–40.
[58] D.A. Almasri, N.B. Saleh, M.A. Atieh, G. McKay, S. Ahzi, Adsorption of phosphate on iron oxide doped halloysite nanotubes, Sci. Rep., 9 (2019) 3232.
[59] A. Jastrzębska, E. Karwowska, D. Basiak, A. Zawada, W. Ziemkowska, T. Wojciechowski, D. Jakubowska, A. Olszyna, Biological activity and bio-sorption properties of the Ti_2C studied by means of zeta potential and SEM, Int. J. Electrochem. Sci., 11 (2016) 2.
[60] A.M. Jastrzębska, J. Karcz, R. Letmanowski, D. Zabost, E. Ciecierska, M. Siekierski, A. Olszyna, Synthesis of RGO/TiO_2 nanocomposite flakes and characterization of their unique electrostatic properties using zeta potential measurements, J. Alloys Compd., 679 (2016) 470–484.
[61] K.S. Sing, R.T. Williams, Physisorption hysteresis loops and the characterization of nanoporous materials, J. Alloys Compd., 22 (2004) 773–782.
[62] M. Naguib, V.N. Mochalin, M.W. Barsoum, Y. Gogotsi, 25th anniversary article: MXenes: a new family of two-dimensional materials, Adv. Mater., 26 (2014) 992–1005.
[63] B. Aïssa, A. Ali, K. Mahmoud, T. Haddad, M. Nedil, Transport properties of a highly conductive 2D Ti_3C_2Tx MXene/graphene composite, Appl. Phys., 109 (2016) 043109.
[64] F. Chang, C. Li, J. Yang, H. Tang, M. Xue, Synthesis of a new graphene-like transition metal carbide by de-intercalating Ti_3AlC_2, Mater. Lett., 109 (2013) 295–298.
[65] Y. Dall'Agnese, M.R. Lukatskaya, K.M. Cook, P.-L. Taberna, Y. Gogotsi, P. Simon, High capacitance of surface-modified 2D titanium carbide in acidic electrolyte, Electrochem. Commun., 48 (2014) 118–122.
[66] Q. Hu, Y. Liu, X. Gu, Y. Zhao, Adsorption behavior and mechanism of different arsenic species on mesoporous $MnFe_2O_4$ magnetic nanoparticles, Chemosphere, 181 (2017) 328–336.
[67] Y. Tian, M. Wu, X. Lin, P. Huang, Y. Huang, Synthesis of magnetic wheat straw for arsenic adsorption, J. Hazard. Mater., 193 (2011) 10–16.
[68] S. Sarkar, L.M. Blaney, A. Gupta, D. Ghosh, A.K. SenGupta, Arsenic removal from groundwater and its safe containment in a rural environment: validation of a sustainable approach, Environ. Sci. Technol., 42 (2008) 4268–4273.
[69] S. Zhang, H. Niu, Y. Cai, X. Zhao, Y. Shi, Arsenite and arsenate adsorption on coprecipitated bimetal oxide magnetic nanomaterials: $MnFe_2O_4$ and $CoFe_2O_4$, Chem. Eng. J., 158 (2010) 599–607.
[70] C. Peng, C.-A. Wang, Y. Song, Y. Huang, A novel simple method to stably synthesize Ti_3AlC_2 powder with high purity, Mater. Sci. Eng. A, 428 (2006) 54–58.
[71] S. Addo Ntim, S. Mitra, Adsorption of arsenic on multiwall carbon nanotube–zirconia nanohybrid for potential drinking water purification, J. Colloid Interface Sci., 375 (2012) 154–159.
[72] X.-J. Gong, W.-G. Li, D.-Y. Zhang, W.-B. Fan, X.-R. Zhang, Adsorption of arsenic from micro-polluted water by an innovative coal-based mesoporous activated carbon in the presence of co-existing ions, Int. Biodeterior, Biodegrad., 102 (2015) 256–264.
[73] S.H. Lee, Y.H. Jang, D.D. Nguyen, S.W. Chang, S.C. Kim, S.M. Lee, S.S. Kim, Adsorption properties of arsenic on sulfated TiO_2 adsorbents, J. Ind. Eng. Chem., 80 (2019) 444–449.
[74] C.M. Elson, D.H. Davies, E.R. Hayes, Removal of arsenic from contaminated drinking water by a chitosan/chitin mixture, Water Res., 14 (1980) 1307–1311.
[75] A. Goswami, P.K. Raul, M.K. Purkait, Arsenic adsorption using copper (II) oxide nanoparticles, Chem. Eng. Res. Des., 90 (2012) 1387–1396.
[76] T. Xu, Y. Cai, K.E. O'Shea, Adsorption and photocatalyzed oxidation of methylated arsenic species in TiO_2 suspensions, Environ. Sci., 41 (2007) 5471–5477.
[77] A. Violante, S. Del Gaudio, M. Pigna, M. Pucci, C. Amalfitano, Sorption and Desorption of Arsenic by Soil Minerals and Soils in the Presence of Nutrients and Organics, Soil Mineral Microbe-Organic Interactions, Springer, 2008, pp. 39–69.
[77] S. Kundu, A.K. Gupta, Arsenic adsorption onto iron oxide-coated cement (IOCC): regression analysis of equilibrium data with several isotherm models and their optimization, Chem. Eng. J., 122 (2006) 93–106.
[79] K.B. Payne, T.M. Abdel-Fattah, Adsorption of arsenate and arsenite by iron-treated activated carbon and zeolites: effects of pH, temperature, and ionic strength, J. Environ. Sci. Health A, 40 (2005) 723–749.
[80] S. Ananta, B. Saumen, V. Vijay, Adsorption isotherm, thermodynamic and kinetic study of arsenic (III) on iron oxide coated granular activated charcoal, Int. J. Environ. Sci., 4 (2015) 64–77.
[81] P. Mondal, C. Balomajumder, B. Mohanty, A laboratory study for the treatment of arsenic, iron, and manganese bearing ground water using Fe^{3+} impregnated activated carbon: effects of shaking time, pH and temperature, J. Hazard. Mater., 144 (2007) 420–426.
[82] M. Islam, R.K. Patel, Evaluation of removal efficiency of fluoride from aqueous solution using quick lime, J. Hazard. Mater., 143 (2007) 303–310.
[83] L. Mihaly-Cozmuta, A. Mihaly-Cozmuta, A. Peter, C. Nicula, H. Tutu, D. Silipas, E. Indrea, Adsorption of heavy metal cations by Na-clinoptilolite: equilibrium and selectivity studies, J. Environ. Manage., 137 (2014) 69–80.
[84] M.E. Argun, S. Dursun, Removal of heavy metal ions using chemically modified adsorbents, J. Int. Environ. Appl. Sci., 1 (2006) 27–40.
[85] M.M. Rahman, M. Adil, A.M. Yusof, Y.B. Kamaruzzaman, R.H. Ansary, Removal of heavy metal ions with acid activated carbons derived from oil palm and coconut shells, Materials, 7 (2014) 3634–3650.